Li, S., Moreno, M., Bedford, J., Rosenau, M., Oncken, O. (2015): Revisiting viscoelastic effects on interseismic deformation and locking degree: A case study of the Peru-North Chile subduction zone. - *Journal of Geophysical Research, 120*, 6, p. 4522-4538.

DOI: http://doi.org/10.1002/2015JB011903

AGU PUBLICATIONS

JGR

Journal of Geophysical Research: Solid Earth

RESEARCH ARTICLE
10.1002/2015JB011903

Key Points:
- Viscoelastic model produces long-wavelength horizontal interseismic deformation
- Elastic model overestimates interseismic locking depth
- Linear viscoelastic inversions are performed using FEM-derived Green's functions

Supporting Information:
- Text S1, Figures S1–S12, and Table S1

Correspondence to:
S. Li,
shaoyang.li@gfz-potsdam.de

Citation:
Li, S., M. Moreno, J. Bedford, M. Rosenau, and O. Oncken (2015), Revisiting viscoelastic effects on interseismic deformation and locking degree: A case study of the Peru-North Chile subduction zone, *J. Geophys. Res. Solid Earth*, *120*, 4522–4538, doi:10.1002/2015JB011903.

Received 24 JAN 2015
Accepted 24 MAY 2015
Accepted article online 28 MAY 2015
Published online 22 JUN 2015

Revisiting viscoelastic effects on interseismic deformation and locking degree: A case study of the Peru-North Chile subduction zone

Shaoyang Li[1], Marcos Moreno[1], Jonathan Bedford[1], Matthias Rosenau[1], and Onno Oncken[1]

[1]Helmholtz Centre Potsdam, GFZ German Research Centre for Geosciences, Potsdam, Germany

Abstract Viscoelastic effects potentially play an important role during all phases of the earthquake cycle in subduction zones. However, most current models neglect such effects in the interseismic deformation pattern. Here we use finite element method (FEM) models to investigate the control of viscoelasticity on interseismic deformation and to highlight the pitfalls of interpreting the data with purely elastic models for both the forward and inverse problems. Our results confirm that elastic models are prone to overestimating the interseismic locking depth, a crucial parameter for estimating the maximum possible earthquake magnitude. The application of the viscoelastic model improves the fit to the interseismic deformation, especially in the inland area. Additionally, we construct 3-D FEM models constrained by geophysical and GPS data and apply our methodology to the Peru-North Chile subduction zone. Our results indicate that viscoelastic effects contribute significantly to the observed GPS data. The signals interpreted as back-arc shortening in the elastic model can be alternatively explained by viscoelastic deformation, which, in turn, dramatically refines the interseismic locking pattern in both dip and strike directions. Our viscoelastic locking map exhibits excellent correlation with the slip distributions of previous earthquakes, especially the recent 2014 *Mw* 8.1 Iquique earthquake. The incorrect elastic assumptions affect the analysis of interseismic deformation with respect to slip deficit calculations. Our results thus suggest that it is necessary to thoroughly reevaluate existing locking models that are based on purely elastic models, some of which attribute viscoelastic deformation to different sources such as microplate sliver motions.

1. Introduction

The advent of space-based geodetic observations in subduction zones is facilitating a better understanding of the short-term seismic cycle behavior and its relation to the long-term tectonic evolution. Traditionally, the seismic cycle deformation has been explained within the framework of the purely elastic rebound theory [*Reid*, 1910]. Following this concept, elastic dislocation models [e.g., *Okada*, 1985, 1992] are commonly employed to analyze and interpret surface deformation related to tectonic mechanisms, such as plate boundary slip, interseismic locking degree, back-arc shortening, sliver motion, and microplate rotation [*Bevis et al.*, 2001; *Brooks*, 2003; *Brooks et al.*, 2011; *Chlieh*, 2011; *Kendrick et al.*, 2001; *Moreno et al.*, 2010; *Nocquet et al.*, 2011; *Wallace et al.*, 2004]. However, there is growing recognition that the viscoelastic behavior of the mantle plays an important role in the deformation throughout a seismic cycle [e.g., *Wang et al.*, 2012]. It has also been shown that viscoelastic relaxation contributes significantly to the short-term and long-term postseismic deformation [e.g., *Hu et al.*, 2014, 2004; *Pollitz et al.*, 2006; *Sun et al.*, 2014]. Thus, the earthquake cycle deformation differs from the elastic rebound in its simplest forms, and reevaluating the interseismic deformation with viscoelastic models is of great importance for correctly decomposing the surface signal and for estimating the stress built up on the locked plate interface.

Modern geophysical measurements allow for reasonable constraints on fault geometry and for material properties of subduction margins [e.g., *Hyndman and Wang*, 1993; *Yuan et al.*, 2000]. Coseismic slip that is supposed to occur on a single or a set of interconnecting fault interface patches with known geometry can be successfully modeled with Green's functions of dislocation in an elastic half-space [*Okada*, 1985, 1992]. Conversely, interseismic fore-arc deformation, which is driven mainly by plate convergence in the presence of a locked subduction megathrust, also affects the whole volume of the margin. Interseismic deformation has been frequently simulated using the normal fault-like back slip model [*Savage*, 1983]. In back slip modeling, it is commonly assumed that interseismic deformation is a mirror image of coseismic deformation, and locking of the two plates is simulated with dislocation along the fault in the opposite sense to the coseismic slip (Figure 1a).

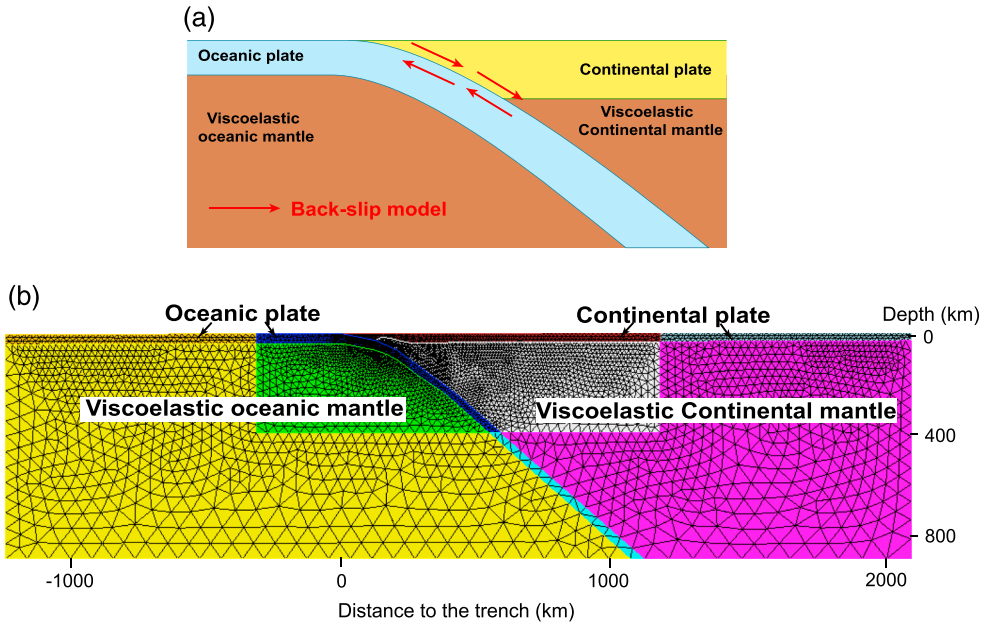

Figure 1. (a) Schematic plot of the "back slip" subduction zone model. The so-called back slip model assumes that the seismogenic zone creeps in the opposite sense of coseismic rupture in the interseismic period (as shown with red vectors). (b) Two-dimensional synthetic FEM model structure. The smaller inner structure has a realistic curved geometry representative of the south-central Chile subduction zone [*Li et al.*, 2014]. The outer blocks were obtained by extending the inner ones and have same attributes as the corresponding extended blocks. Therefore, the model is only composed of four homogenous blocks.

The purpose of this paper is to investigate how viscoelasticity affects the interseismic deformation and thus the estimation of locking degree in subduction zones. To address this problem we construct finite element method (FEM) models of the subduction zone and generate FEM-derived Green's functions. We start with 2-D synthetic modeling in order to compare features of elastic and viscoelastic models. Next we investigate the locking depths recovered from both elastic and viscoelastic forward models and validate these results with a linear viscoelastic inversion method. Finally, we apply our methodology to a 3-D case study of Peru-North Chile, in the segment of the 2014 *Mw* 8.1 Iquique event [*Hayes et al.*, 2014; *Schurr et al.*, 2014], using published GPS data. We investigate the viscoelastic effects measured in the GPS data by means of forward modeling and inversion with both elastic and viscoelastic models. We compare the characteristic differences between viscoelastic and elastic locking maps and compare these locking maps to the known slip distributions of recent and historical ruptures along this subduction margin.

2. 2-D FEM Model Configuration

To investigate the major differences between viscoelastic and elastic models, we create synthetic 2-D FE-models. All numerical simulations in this study are solved with the finite element modeling software PyLith [*Aagaard et al.*, 2013]. In our models we consider oceanic and continental plates that are defined as purely elastic bodies extending to the depths of respective estimated elastic thicknesses. Below the plates we consider the lithospheric and asthenospheric mantles to be isotropic mantle domains. These mantle domains have purely elastic properties in the elastic models and viscoelastic properties in the viscoelastic models. Hence, our simplified 2-D models consist of four domains (Figure 1): (1) continental plate, (2) viscoelastic continental mantle, (3) oceanic plate, and (4) viscoelastic oceanic mantle.

Our synthetic model is representative of an average profile across the geophysically constrained, curved geometry of the south-central Chile subduction zone (inner small mesh in Figure 1b) [*Groß et al.*, 2008; *Haberland et al.*, 2009; *Tassara and Echaurren*, 2012]. We expand our realistic geometry 1000 km east, 1000 km west, and 500 km deep (Figure 1b), in order to minimize the boundary effects of simulation, especially the viscoelastic flow of the upper mantle. The elastic thickness of the oceanic plate is set to 30 km following estimates of *Contreras-Reyes and Osses* [2010] for this area. The refined portion of the

mesh is 1614 km wide and 400 km deep. Therefore, in total the mesh is 3614 km wide and 900 km deep. Moreover, we use controlled meshing to gradually change the size of the elements in our model (Figure 1b), thus resulting in 5593 triangle elements inside the inner smaller mesh out of the total 9002 elements in the larger mesh. The discretization size of the mesh is about 1 km in the fore arc and 60 km in the mantle. The larger mesh is used for the entire simulation. However, only the outputs from the smaller mesh are used in our analyses [e.g., *Li et al.*, 2014].

Our interseismic model neglects gravity because it deals with stress changes as perturbations to the absolute state of stress. These stress perturbations are simulated by kinematically specifying back slip rate along the fault interface, while the lateral boundaries and base of the problem domain are fixed to have zero displacement in horizontal direction and vertical direction, respectively. The resulting strain is thus accumulated in the continental plate due to the fault slipping along the plate interface and due to mantle viscoelastic relaxation. The accumulated displacements on the FEM nodes are calculated with respect to their original locations within an assumed Cartesian coordinate system.

Studies of the Earth's response to sudden stress changes of large earthquakes indicate that viscous flow in the lower crust and upper mantle during a short postseismic period can be characterized by a transient nonlinear rheology, such as a power law [*Freed and Burgmann*, 2004; *Kirby and Kronenberg*, 1987] or Burgers rheology [*Peltier et al.*, 1981; *Pollitz et al.*, 2008]. However, for decadal or longer time scales a simple linear Maxwell rheology is most frequently employed, such as in Glacial Isostatic Adjustment, modeling of delayed mantle response of glacial retreat [e.g., *Mitrovica*, 1996], and in viscoelastic relaxation simulation related to earthquake cycle at decadal time scales [e.g., *Hu et al.*, 2004]. In this study, we are dealing with a decadal to century time scale of interseismic viscoelastic response of the Earth. Therefore, we choose to ignore transient rheology and incorporate Maxwell viscoelastic rheology. The Maxwell rheology is a combination of time-independent elastic behavior and time-dependent viscous behavior, characterized by elastic modulus and viscosity, respectively [*Christensen*, 1982]. Our model incorporates viscosities of $4 \times 10^{19} Pa \times S$ and $1 \times 10^{20} Pa \times S$ for viscoelastic continental mantle and viscoelastic oceanic mantle, respectively, corresponding to Maxwell relaxation times of approximately 20 and 50 years, respectively (relaxation times are defined as the viscosity divided by the rigidity, where the rigidity value of both the oceanic and continental mantles is 64 GPa). The linear behavior of the Maxwell rheology complies with the assumptions of linear viscoelastic inversion (shown in section 5). In these models, mantle viscosity values are assumed from the results of previous studies in south-central Chile [*Hu et al.*, 2004; *Moreno et al.*, 2011].

3. Clarifying Viscoelastic Effects on Surface Deformation

In order to clarify the characteristics of the viscoelastic response on surface deformation, we conduct two forward back slip models: (1) elastic and (2) viscoelastic. In the two models we implement the same model configuration, boundary conditions, elastic material properties, and fault locking state. For simplicity, we apply to all models a uniform full locking of the fault interface from 0 to 50 km depth without a transition zone between fully locked and freely creeping zones [e.g., *Chlieh*, 2004]. We apply the full plate convergence rate of 68 mm/yr [*Ruegg et al.*, 2009] along the slab-top fault from 0 to 50 km depth in the back slip model. Accordingly, the only difference between the elastic and viscoelastic models is either elastic or viscoelastic domains underlying the elastic crustal domains. Elastic properties (e.g., Young's modulus, Poisson's ratio, and density) of viscoelastic materials are assigned to be the same as those of the elastic materials in the corresponding bodies. The material properties used in the modeling and their corresponding references are described in Table S1 in the supporting information.

For the elastic model, a single time step corresponding to 1 year is simulated for annual surface displacement velocities due to time-independent (instantaneous) deformation behavior of the elastic model. In contrast, for the viscoelastic model that exhibits time-dependent deformation behavior, we simulate 200 years of locking using an adaptive time step approach. This approach returns a stable time step based on the constitutive model and rate of deformation [*Aagaard et al.*, 2013] with a maximum permissible time step of 2 years, thereby capturing the stable responses from the viscoelastic materials. For the viscoelastic model, surface velocities are calculated from the last time step of the simulation because the viscoelastic response after this time (i.e., about 10 times the Maxwell relaxation time [*Hu et al.*, 2004]) has stabilized, and therefore, the velocities can be representative of those in the late interseismic stage.

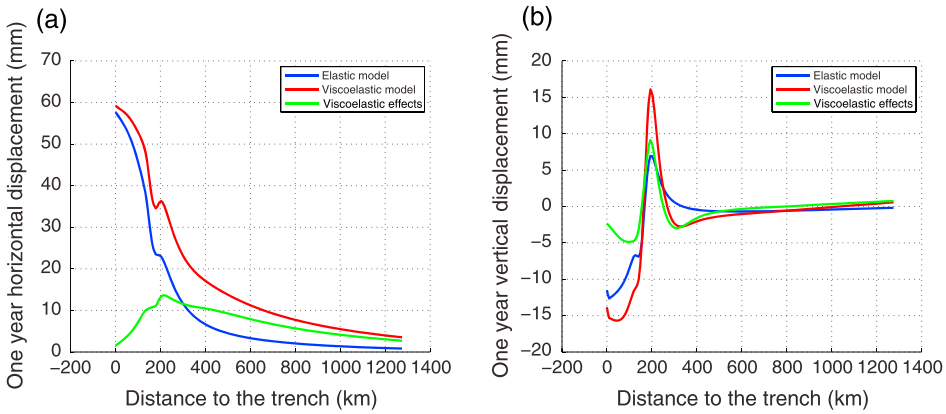

Figure 2. The viscoelastic effects of surface deformation from the back slip model. Note that both continental and oceanic mantles were given viscoelastic behaviors in the viscoelastic models. The red curves are the results of the viscoelastic models. The blue curves are the results of the elastic models. The green curves are the difference between viscoelastic and elastic models, effectively showing the impact of viscoelastic deformation on the predicted displacements. (a) The viscoelastic effects for horizontal displacement and (b) the viscoelastic effects for vertical displacement are shown.

The interseismic viscoelastic effects on horizontal and vertical surface deformation are shown in Figure 2. In general, the elastic and viscoelastic models produce qualitatively similar deformation patterns but show quantitative differences with significantly different magnitudes of displacement in both horizontal (Figure 2a) and vertical (Figure 2b) directions (>10% of plate convergence). The viscoelastic models produce a much (~100 km) broader deformation than the elastic models as shown by horizontal displacements that extend much further inland with differences of about 10 mm/yr in the back arc. The highest deviation in horizontal deformation between the viscoelastic and elastic models is found at 200 km from the trench and amounts to 20% of plate convergence. In the vertical direction, the viscoelastic models in comparison to the elastic models subside by as much as 5 mm/yr faster between 0 and 100 km from the trench and uplift by as much as 9 mm/yr faster at just over 200 km from the trench.

An alternative kinematic model for simulating interseismic deformation is the so-called Subducting Plate model (Figure S1 in the supporting information) [e.g., *Chlieh*, 2004; *Kanda and Simons*, 2010]. Although this model may predict interseismic elastic deformation that is similar to that of the back slip model [*Kanda and Simons*, 2010], the difference between these models in their predictions of interseismic viscoelastic deformation is not clear. In Text S1 in the supporting information, we detail the comparison between the back slip and plate model approaches. Our results confirm that these two models predict similar deformation patterns in both the elastic and viscoelastic simulations and also indicate that the choice of subduction model produces negligible differences in surface deformation with respect to the differences between elastic and viscoelastic modeling approaches (Figure S2).

In summary, viscoelastic models predict higher magnitudes of deformation in the late stages of the interseismic period than those predicted by the purely elastic model. In the elastic model, the shortening of the upper plate is only due to the elastic processes of fault locking, whereas in the viscoelastic model, a portion of the stress built up by fault locking is relaxed in the viscoelastic domains causing additional viscous deformation on the surface that is expressed as a longer wavelength signal. Additionally, the surface points that are most sensitive to the viscoelastic effects of interseismic locking are found in the near field (close to the trench) and in the far field.

4. Interpreting Viscoelastic Deformation With Elastic Models

In order to demonstrate the pitfalls of interpreting viscoelastic deformation and estimating the width of the locked zone with a purely elastic dislocation model, we develop a modeling strategy consisting of two steps: (1) simulate a viscoelastic forward model with uniform full locking down to 30 km depth for 200 years and (2) calculate elastic forward models with different uniform full locking depths. In these models, the locking depth varies between 20 km and 60 km in 5 km increments (nine locking depths tested). Finally, we compare the resulting surface deformations of the elastic models with that of predefined locking depth of the viscoelastic model.

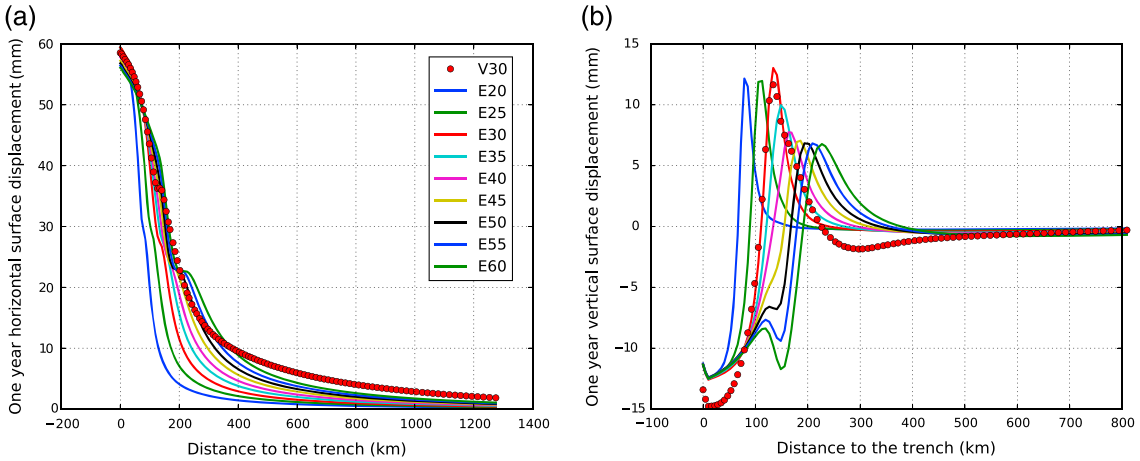

Figure 3. (a) Horizontal displacement fitting of the viscoelastic synthetic deformation with elastic models. The red dotted curve is the result from the viscoelastic model. The solid lines are the results from elastic models. In the legend, the letters V and E stand for viscoelastic model and elastic model, respectively. The number on the legend denotes the locking depth of the corresponding simulation. (b) Vertical displacement fitting of the viscoelastic synthetic deformation with elastic models. The legend is same as Figure 3b.

The surface displacement of the viscoelastic model and the group of elastic models are shown in both horizontal and vertical directions in Figure 3. In the horizontal direction (Figure 3a), the elastic model with 30 km uniform locking depth starts to deviate from the viscoelastic prediction for the same locking depth from a distance of about 50 km from the trench to the far field. However, the elastic model with 50 km uniform locking depth best fits the viscoelastic model, especially in the domain of 50 to 300 km from the trench. Therefore, if one were to invert only horizontal displacement for locking degree, as commonly done, the best fitting locking depth from elastic models would be incorrectly determined at around 50 km (as shown by the best fit curve in Figure 3a) as compared to the true locking depth of 30 km.

In the vertical direction (Figure 3b), the elastic model with 30 km uniform locking depth fits the viscoelastic model very well between 50 and 200 km from the trench. Yet none of the elastic models can reproduce the vertical signal of the viscoelastic model in the far field as well as close to the trench (about 0 to 50 km), where the effect of the continental and oceanic mantle flow is felt most strongly. Therefore, if one were to invert only vertical displacement for locking degree using elastic models, the best fitting locking depth would be 30 km, which is close to the true value.

In summary, elastic models reproduce neither the horizontal nor the vertical displacement of the viscoelastic model in the far field. Elastic models can partially fit both horizontal and vertical displacements of the viscoelastic model in the near field with respect to the trench, and the elastic model requires deeper fault locking depth to fit the viscoelastic horizontal deformation. Therefore, we are demonstrating that the use of an elastic model for estimating locking is likely to overpredict the apparent locking depth, due to the fact that viscoelastic deformation is being incorrectly modeled as elastic. Since most of the current inversions for locking degree in subduction zones have used purely elastic assumptions [e.g., *Moreno et al.*, 2011; *Ruegg et al.*, 2009], it is likely that the locking depths have been systematically overestimated, requiring a review of these models for better estimation of potential magnitude of the upcoming earthquakes.

5. Linear Viscoelastic Inversion

Next we develop an inversion method for estimating the locking degree based on a viscoelastic model. Our inversion method is linear, because of the linear relationship between fault slip rate and surface deformation rate (linear in time) and also because of the independence of slip of different fault patches on the surface deformation (linear in space). In the late stage of the interseismic period, the viscoelastic response from the previous great earthquake has diminished to a negligible amount due to its recurrence period (in the order of 100 years) that is larger than the characteristic Maxwell decay time for such an earthquake (in the order of tens of years for the generally assumed range of viscosities of the viscoelastic mantle and the range of stresses induced by megathrust events).

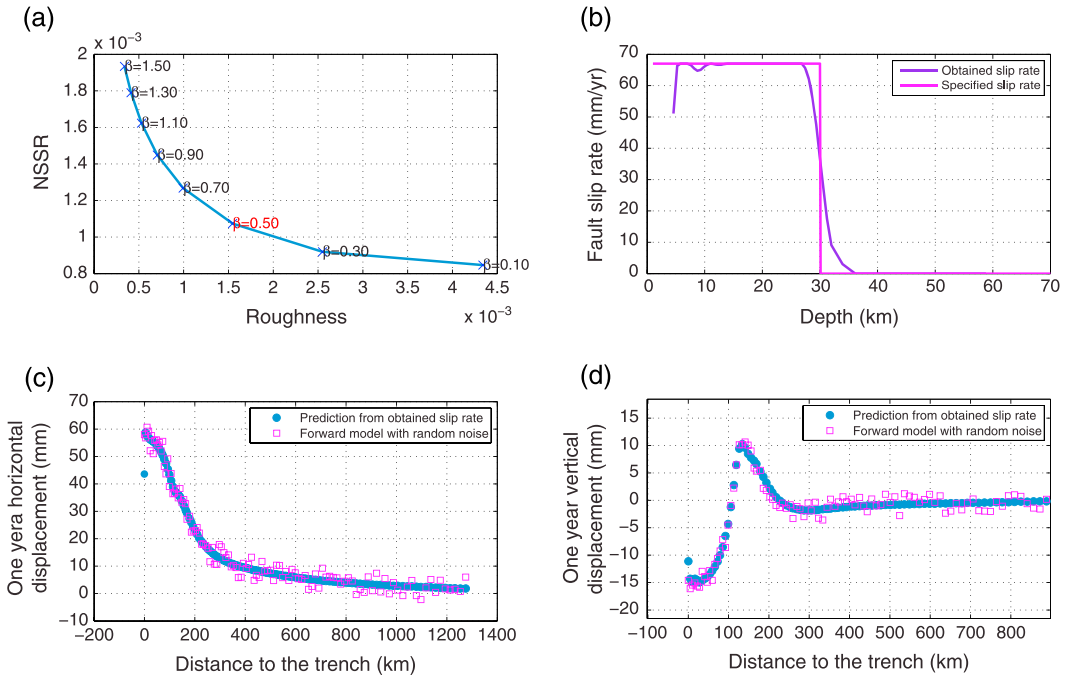

Figure 4. Viscoelastic inversion results of the deformation that was forward modeled with a viscoelastic model. Random noise has been added to the forward modeled displacement rates. (a) NSSR (the sum of squared residuals normalized by the data standard errors) plotted against the model roughness. (b) The specified slip rate in the forward viscoelastic model and the obtained slip rate from the inversion of synthetic data using FEM-derived Green's functions. (c) Horizontal displacement rates from the viscoelastic forward model with manually added random noise and the prediction of slip rate obtained from the inversion of synthetic data. (d) Vertical displacement rates from the viscoelastic forward model with manually added random noise and the prediction of the slip rate obtained from the inversion of synthetic data.

To demonstrate the validity of ignoring the effects of previous earthquakes, the horizontal and vertical displacement velocities of four forward models with the same interseismic loading in the late stages of the 200 years are plotted as a function of time at four points along the continental plate surface (Figures S3 and S4). These simulations are repeated, with identical boundary conditions except for the introduction of a sudden stress change at the beginning of the simulation to account for the postseismic viscoelastic relaxation of the last megathrust event (Figures S5 and S6). The plots clearly show that for models both with and without the prior earthquake, the horizontal and vertical velocities along the continental plate surface are constant and equivalent in the late simulation time. This indicates a linear relationship between surface deformation rate and specified fault creeping rate in our viscoelastic models.

Given that there is a linear surface deformation rate in the late interseismic period of our models, a linear viscoelastic inversion for the plate interface back slip rate with FEM-derived Green's functions can be constructed following the technique according to *Masterlark* [2003]. The relationship between surface deformation rate and slip rate along the fault is expressed by the linear system:

$$G^*s = d \tag{1}$$

where G is the Green's function matrix, s is the unsolved slip rate vector, and d is the surface deformation rate vector in the late stages of the interseismic period. The matrix G is determined by the model geometry, the time-dependent and time-independent components of material properties, and the meshing of the FEM model, again following the technique of *Masterlark* [2003].

We used the MATLAB routine lsqlin, a subspace trust-region method based on the interior-reflective Newton method described by *Coleman and Li* [1996], to solve the regularized version of equation (1). Minimum and maximum slip rate constraints are applied to avoid outcomes with unreasonable slip rate patterns and to improve the model resolution [*Du et al.*, 1992; *Harris and Segall*, 1987]. No additional constraints are imposed at the updip and downdip limits of locking. To test the possible occurrence of

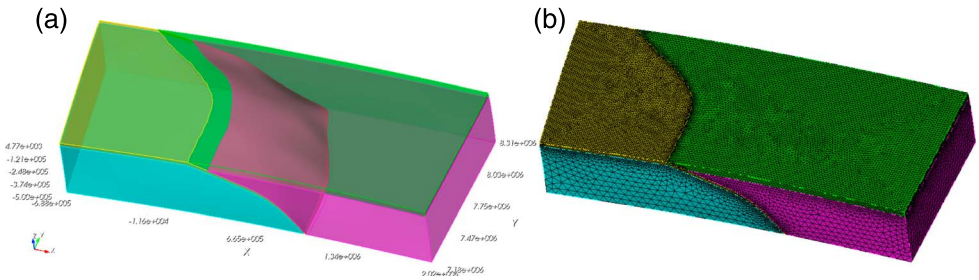

Figure 5. Three-dimensional FEM model configuration. (a) Model incorporates precise geometry of the slab and continent Moho, which were derived from geophysical observations. The model structure consists of four domains including elastic continental and oceanic plates, and viscoelastic continental and oceanic mantles. (b) Model has finer mesh size close to the slab, upper surface, and the trench and coarser mesh size in deep continental and oceanic mantle.

inverted deep slip, all fault nodes located above a reasonable depth (we use 70 km in our study) are employed in our inversion. The smoothing parameter β is estimated from the trade-off curve between misfit and slip rate roughness. The selected value is obtained in the inflection of the curve (e.g., Figure 4a for our 2-D viscoelastic inversion) and gives an optimal balance between data fit and model roughness [*Bürgmann et al.*, 2005; *Du et al.*, 1992].

In our 2-D synthetic model, we use 0 and 70 mm/yr (slightly larger than the plate convergence rate for south-central Chile) as minimum and maximum slip rate constraints, respectively. The Green's functions are calculated between 0 and 70 km depth on the plate interface based on the back slip model that includes the surface deformation rate of a background viscoelastic deformation. In order to test the performance of the FEM-derived viscoelastic Green's functions, data-independent random noise is added to the synthetic data predicted by the forward viscoelastic model with uniform full locking to 30 km depth. The inversion results are summarized in Figure 4. The sudden change of slip rate around 30 km depth is well resolved in our inversion (even with added noise). Our favored inversion (see trade-off curve on Figure 4) recovers well the main features of the fault back slip rate of the forward model. The predicted surface deformation rate (G^*s) from the obtained back slip model fits well the forward modeled deformation with random noise in both the horizontal and vertical directions (Figures 4c and 4d), which, again, corroborates the validity of our viscoelastic inversion method.

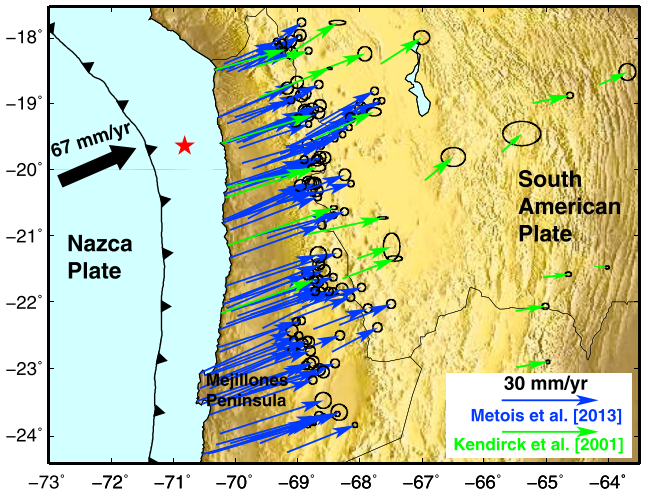

Figure 6. Published interseismic GPS data sets in the North Chile subduction zone. The green velocities are from published data of *Kendrick et al.* [2001]. The blue vectors are data from *Métois et al.* [2013]. The red star indicates the epicenter of 1 April 2014, *Mw* 8.1 Iquique earthquake.

6. 3-D Analysis of Interseismic Deformation of North Chile Before 2014 Iquique

In this section we use a 3-D FEM (Figure 5) and published GPS velocities (Figure 6) [*Kendrick et al.*, 2001; *Métois et al.*, 2013] to explore the viscoelastic effect on interseismic deformation along the Peru-North Chile subduction margin. Due to the density of GPS measurements covering the late stage of the megathrust interseismic phase [*Chlieh*, 2011; *Comte and Pardo*, 1991] at various distances to the trench, this margin is our chosen case study to demonstrate the efficacy of estimating locking using viscoelastic Green's functions. Furthermore, there is a well-documented record of coseismic slip models along this margin, most recently for the *Mw* 8.1 2014 Iquique earthquake

[*Hayeset al.*, 2014; *Schurr et al.*, 2014], which can be compared to our final locking model. In order to compare our result with previous studies for the study area, we use the published plate convergence [*Angermann et al.*, 1999] to convert the back slip rate map into a locking degree map. Although this model is specifically for the Peru-North Chile margin, the methods presented could be applied to better understand deformation patterns in other subduction zones.

6.1. Model Setup and GPS Data

Previous studies indicate that the fault geometry can greatly affect the predicted surface deformation and the obtained slip distribution on the fault interface [e.g., *Moreno et al.*, 2009]. In order to avoid introducing artifacts from the simplified fault geometry, we use a geophysically constrained geometry in our 3-D FEM models, which incorporates not only the geometry of the subduction slab but also topography, bathymetry data, and the continental Moho (Figure 5) [*Contreras-Reyes and Osses*, 2010; *Hayes et al.*, 2012; *Schurr et al.*, 2009; *Tassara and Echaurren*, 2012]. The structure of our 3-D model consists of four blocks (Figure 5a): continental plate, viscoelastic continental mantle, oceanic plate, and viscoelastic oceanic mantle, similar to the 2-D synthetic model (Figure 1).

In order to avoid boundary effects, we employ a model significantly larger than our study area. The model space is about 2700 km long, 1100 km wide, and 500 km deep (Figure 5a). We use controlled meshing to gradually change the size of the elements in the areas of interest. The final mesh is composed of 510,386 tetrahedral elements in total, with finer element discretization sizes on the continental surface (about 5 km), near to the oceanic slab (about 10 km), and near to the trench (about 1 km). A coarser element discretization size is assigned to the deep parts of both mantles (from about 50 km) (Figure 5b). Mesh size is chosen with the following considerations: (1) ill-conditioned problems can be avoided when constructing the relation between fault slip and surface deformation; (2) fault creep and variation of material properties will be better resolved close to the oceanic slab; (3) highly distorted elements, which would result in nonconverging solutions and numerical errors, can be avoided close to the trench; and (4) computational time and cost can be saved without affecting resolution accuracy by using coarse elements in deep mantle.

As was the case with the 2-D models, the east and west boundaries and base of the problem domain of our 3-D models are fixed to have zero displacement in horizontal direction and vertical direction, respectively. The plate convergence at this margin is 67 mm/yr with an obliquity of approximately 18° from the normal direction of the trench [*Angermann et al.*, 1999; *Kendrick*, 2003]. We use this convergence velocity as the reference for simulating back slip rate of fully locked plate interface and calculating obtained locking degree. The published GPS observations in the study area are mainly based on survey-mode GPS data and therefore do not include the vertical interseismic displacements. The GPS data set is composed of 130 horizontal velocity vectors (Figure 6) published by *Métois et al.* [2013] (data for the period 2008–2012) and *Kendrick et al.* [2001] (data for the period 1993–2001). All velocities are defined with respect to a stable South American reference frame and thus comparable to the deformation predicted by FEM models. The data set spans from latitude 18°S to 24°S, longitude −72°E to −64°E therefore as far as roughly 350 km from the trench. Most of the GPS data are located near the coast in the fore arc, with some data distributed sparsely in the back arc. The use of these data allows us to directly compare our viscoelastic locking prediction with previously published elastic models.

6.2. Forward Modeling

In order to achieve a first-order relationship between GPS observations and elastic as well as viscoelastic predictions, we perform eight forward scenarios by changing the depth of a uniform locked zone from 30 km to 80 km, for both elastic and viscoelastic 3-D models. We quantify the misfit between the observations (obs) and FEM model predictions (pred) using a weighted root-mean-square of the residuals (WRMS) criterion defined as

$$\mathrm{WRMS} = \sqrt{\frac{\sum_{i=1}^{n}\left(\frac{\mathrm{obs}_i - \mathrm{pred}_i}{w_i}\right)^2}{\sum_{i=1}^{n}\left(\frac{1}{w_i}\right)^2}} \tag{2}$$

where n is the number of observations, $(\mathrm{obs}_i - \mathrm{pred}_i)$ and w_i are respectively the residual and the weighting uncertainty in the measurements assigned to the ith velocity component.

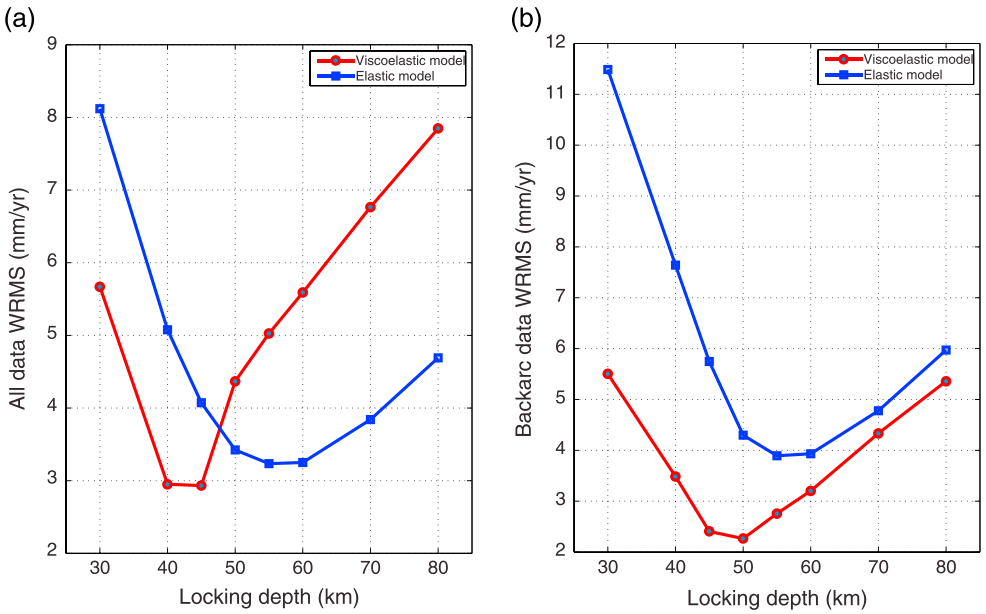

Figure 7. Comparison of the WRMS misfit curves from forward elastic and viscoelastic models with varied uniform locking depth extending from the trench. (a) The values of WRMS misfit are calculated based on all GPS horizontal observations. (b) The values of WRMS misfit are calculated based on back-arc GPS horizontal observations. The blue curve with solid squares represents the elastic models. The red curve with solid circles represents the viscoelastic models.

We plot the WRMS misfit as a function of uniform full locking depth, taking into accounts all of the GPS observations (Figure 7a). The minimum WRMS is reached for the elastic model where the locking depth extends to 55 ± 5 km and for the viscoelastic model where the locking depth extends to 45 ± 5 km. In other words, the viscoelastic model is capable of fitting all the GPS data with a shallower downdip termination of locking than in the elastic model, which is consistent with our explorative 2-D synthetic simulations. Moreover, the viscoelastic model improves the fit to the GPS: The improvement in fit is because the long-wavelength signal seen in the data can be better reproduced by the viscoelastic model than by the elastic model. Additionally, the optimal downdip end of locking of the viscoelastic model is in a better agreement with the seismogenic depth range (45 ± 5 km for this region found by seismological studies [*Comte et al.*, 1994; *Schurr et al.*, 2014, 2012]) than that of the elastic model.

In order to compare the misfit of elastic and viscoelastic models in just the far field (where the viscoelastic effects are more distinguishable as indicated by our 2-D synthetic models in section 3) the WRMS values are calculated for a subset of far-field stations (Figure 7b). In this case, we define the far field at longitudes east of 69°W. In order to best fit the surface deformation in the far field, the elastic model requires a deeper locking depth than the viscoelastic model. Moreover, the viscoelastic model surpasses the elastic model with better overall fitting of GPS data; i.e., all viscoelastic models have smaller misfit value than elastic models with the same locking depth (Figure 7b). Therefore, the viscoelastic effects in the interseismic deformation are very likely already being observed in the modern geodetic data, especially for the back-arc region. Note that in this section we employ fixed viscosity values for both continental (i.e., $4 \times 1019 Pa \times S$) and oceanic mantles (i.e., $1 \times 1020 Pa \times S$); therefore, we perform sensitivity testing of viscosity for the continental mantle and we present these results in more detail in the discussion section.

The residuals between the GPS velocities and the predicted velocities from the elastic and viscoelastic models (55 and 45 km locking termination depths, respectively) are plotted in Figures 8a and 8b. In Figure 8a, the elastic model overestimates the magnitude of GPS displacements close to the trench (residual vectors point trenchward for the near-field stations) and underpredicts the GPS in the far field (residual vectors point landward in the back arc). The viscoelastic model better reproduces the GPS vectors with smaller magnitude

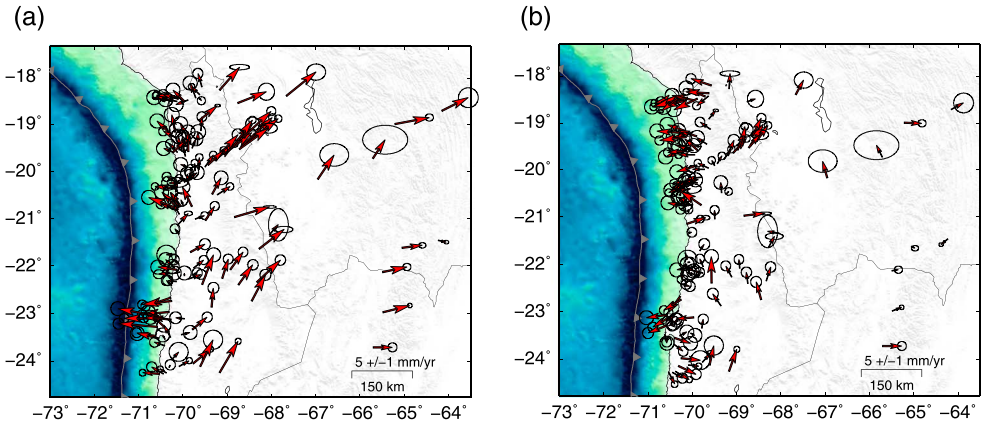

Figure 8. The residuals from fitting GPS data with uniformly locked elastic and viscoelastic models. (a) Best elastic fitting model corresponding to 55 km locking depth. (b) Best viscoelastic fitting model corresponding to 45 km locking depth.

residuals that point in seemingly random directions (Figure 8b), suggesting that the surface deformation can be better explained by subduction-related viscoelastic processes. In both models the patterns of residual vectors, especially those residuals that point in trench parallel directions, suggest that there is significant along-strike variation in the locking degree that would be better modeled with an inversion approach.

6.3. Elastic and Viscoelastic Inversion of Locking Degree

As viscoelastic effects are contained in the geodetic data, it is necessary to make a viscoelastic inversion based on GPS data. We calculate FEM-derived Green's functions for both viscoelastic and elastic models (as described in section 5). In order to reasonably decrease computational cost, we group nearby fault nodes as nonoverlapping patches with a size of about 20 km^2 [*Masterlark*, 2003; *Masterlark and Hughes*, 2008]. An example of three patches in map view is shown in Figure S7. In this way, we achieve an accurate FEM resolution with dense nodes along the fault but a faster calculation of the inversion with larger fault patches. The Green's functions are calculated between 0 and 80 km depth on the plate interface and represent the velocities in the final year of a 200 years long simulation of back slip. During the inversion, no back slip constraints are imposed near the updip limit (i.e., back slip is allowed right up to the trench) and a back slip rate of 0 mm/yr is applied on the fault patches deeper than 70 km depth to avoid unphysical shallow and deep locking and to obtain more stable inversion solutions. For the dip direction, we use 0 and 70 mm/yr as minimum and maximum slip rate constraints; for the strike direction, we used 0 and 30 mm/yr as minimum and maximum slip rate constraints.

The best fitting elastic and viscoelastic inversion results, using the same imposed smoothing constraints, are shown in Figure 9. The elastic model requires deep (up to 70 km depth or even deeper if the deeper part of the plate interface had not been assigned zero back slip) and large back slip magnitude to fit all the GPS data (Figure 9a). Residuals of the elastic model are very large (>10 mm/yr in the back arc), even for the best fitting model (Figure 9b), and they show a consistent pattern with an east-west direction. The residuals close to the coast point to the trench indicating elastic model overestimation of the deformation there, while the residuals in the back arc point landward showing that the elastic model underestimates the deformation there.

For the viscoelastic model the residuals in the back arc are considerably less than for the elastic model (Figure 9c). For the viscoelastic model, the back slip distribution from the inversion does not need deeper back slip on the plate interface and the downdip limit of the locked zone is restricted to a maximum of 50 km depth (Figure 9c). The total amount of back slip needed to fit all the GPS data for the viscoelastic model is much less than that for the elastic model. Hence, the back slip pattern of the viscoelastic model is more patchy in both dip and strike direction. Additionally, the viscoelastically derived locking shows more heterogeneity in the margin-lateral locking distribution and generates a better fit to the GPS data (Figure 9d).

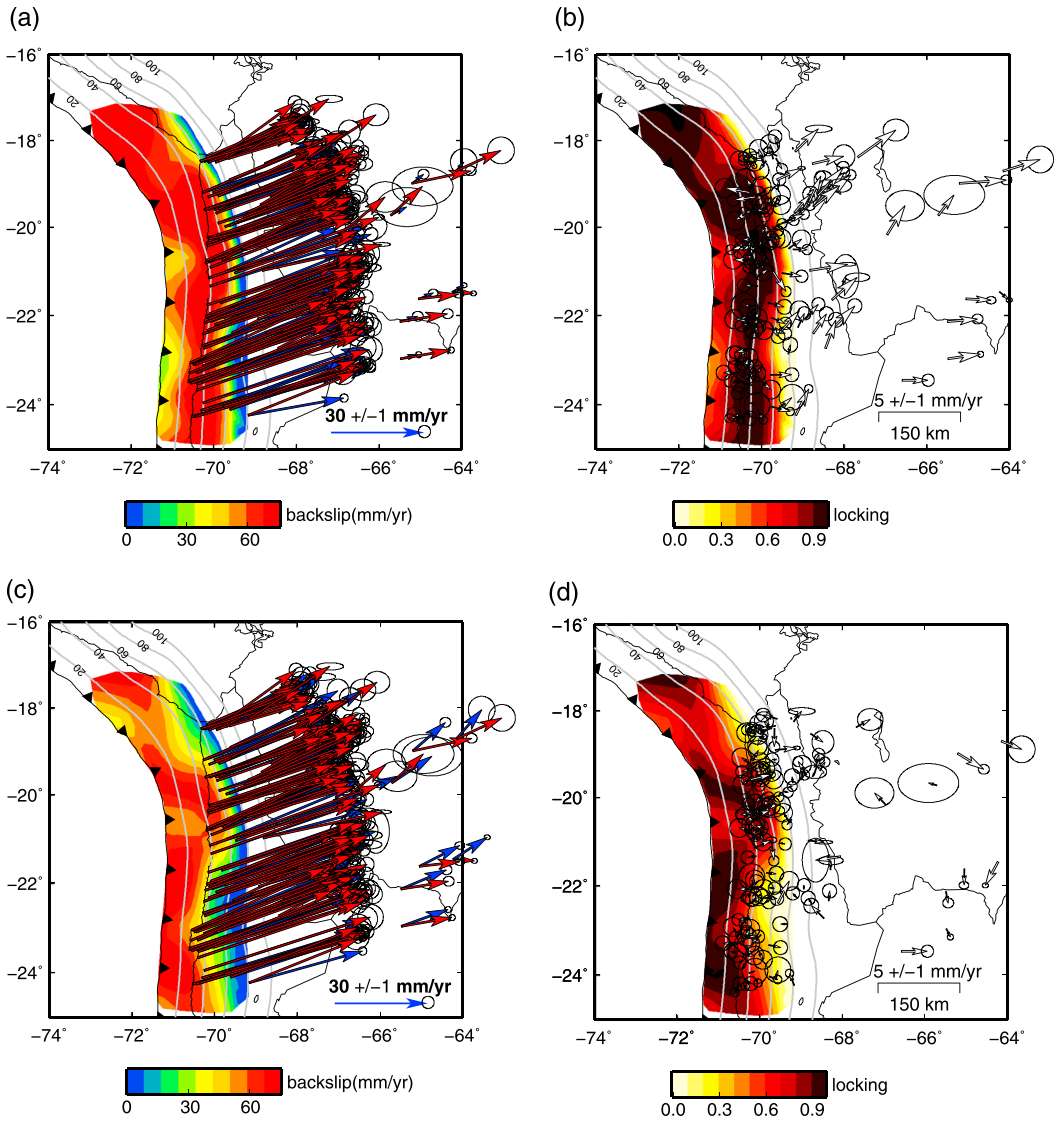

Figure 9. Comparison of best fitting elastic and viscoelastic inversion results for the same imposed smoothing constraint. (a) Determined back slip distribution with elastic Green's functions. The red vectors are published GPS data used in our case study. The blue vectors are predicted deformation from the inverted back slip distribution. (b) Locking map of our case study area obtained by the elastic model, representing the ratio between back slip and long-term convergence rates. The white vectors with black outlines are the residuals from the GPS observations and predictions of inverted slip. (c) Determined back slip distribution with the viscoelastic Green's functions. The red vectors are published GPS data used in our case study. The blue vectors are predicted deformation from the inverted back slip distribution. (d) Locking map of our case study area obtained by the viscoelastic model, representing the ratio between back slip and long-term convergence rates. The white vectors with black outlines are the residuals from the GPS observations and predictions of inverted slip. In all the four panels, the gray solid contours are the isodepths of the subduction interface (the values are given in kilometer).

7. Discussion

7.1. Viscoelastic Interseismic Deformation and Influence of Mantle Viscosity

The locking models that consider viscoelastic behavior shown in this study should be interpreted with caution due to the assumptions that we have made for the modeled subduction zone rheology and mantle flow behavior. In reality, there could be significant heterogeneities in these parameters (which are largely unknown), and inclusion of such heterogeneity into our modeling would go far beyond the scope of this investigation.

The use of Maxwell rheology has been found adequate in modeling decadal to century-long deformation viscoelastic relaxation [*Hu et al.*, 2004; *Wang et al.*, 2012]. The Maxwell rheology instantaneously responds (with elastic behavior) to the stress perturbation induced by an earthquake and by the interseismic contraction and subsequently flows (with viscous behavior) to relieve imposed shear stresses [e.g., *Hu et al.*, 2004; *Thatcher and Rundle*, 1984]. The model produces a time-dependent interseismic deformation; eventually, reaching a steady deformation rate after the relaxation time of the viscoelastic materials has elapsed. The chosen continental mantle viscosity for our modeling influences the magnitude and spatial characteristics of the predicted viscoelastic response and therefore must be carefully selected. In the presented models of this study we use a viscosity within one order of magnitude of $10^{19} Pa \times S$, which has been observed from samples of outcrops [e.g., *Ivins and James*, 1999] and other modeling of geodetic data [e.g., *Hu et al.*, 2014; *Moreno et al.*, 2011]. Additionally, we test a broad range of viscosities for the continental mantle between 1 to $7 \times 10^{19} Pa \times S$, and an additional value of $1 \times 10^{20} Pa \times S$ for our model setup and data set to estimate that the sensitivity of the data is fitting to variations in viscosities of the mantle. The viscoelastic effects are significant in the back-arc; hence, we calculate the WRMS of fitting the back-arc GPS data as a function of uniform locking depth (Figure S8a). The increasing of viscosity in continental mantle results in worse fitting of back-arc GPS data for shallow ($<$45 km) uniform-locking models and better fitting of back-arc GPS data for deep ($>$45 km) uniform-locking models in comparison with the purely elastic model. In order to determine the optimal viscosity value for the continental mantle, we calculate the average WRMS values of physical locking depths (i.e., 40, 45, 50, and 55 km) for all the models with different viscosities. The averaged WRMS values are plotted as function of viscosity (Figure S8b). The averaged WRMS value reaches its minimum around 4×10^{19} and increases again. Hence, we use this optimal value in the following modeling (sections 7.1 and 7.2).

Purely elastic models cannot produce a long-wavelength deformation signal large enough to be observed in the back arc, restricting the interseismic compression to mainly the fore arc. Thus, if one were to interpret viscoelastic interseismic deformation with an elastic model, one would underestimate the deformation in the back arc and/or overestimate the deformation in the fore arc. This has a clear impact when geodetic data are used to invert the depth of the locking zone. Thus, elastic models incorrectly need a deeper downdip limit of the locked zone to reproduce the observed deformation [see *Wang et al.*, 2012]. This can result in an overprediction of slip deficit when locking maps are used for seismic hazard.

In some cases, the lack of a good fit to back-arc velocities by elastic models has been suggested as to indicate long-term, secular back-arc shortening [e.g., *Chlieh*, 2011; *Métois et al.*, 2013]. Indeed, the assumed back-arc shortening and sliver motion can be corrected for with a joint modeling of locking and microplate motion [e.g., *McCaffrey*, 2002]. While it is very likely that some signal in the back-arc may be due to the long-term geological shortening, as observed in the geological record [e.g., *Hindle et al.*, 2002; *Oncken et al.*, 2012], the magnitude of this shortening may be overestimated with a purely elastic model that neglects viscoelastic effects. Furthermore, in future investigations, the parameters defining block rotations of microplates and sliver motion will also have to consider the viscoelastic effects of locking in the joint modeling of locking and microplate/sliver motions.

7.2. Time Dependency of Viscoelastic Model, Influence of Stress Relaxation From Previous Earthquake and Model Spin-Up Effects

The characteristic relaxation time of the deformation between great earthquakes depends on the size of the earthquake [*Wang et al.*, 2012]. Following this relaxation time, the fault locking related deformation becomes dominant. However, the decay to a steady deformation is reached at different times depending the distance to the trench. One implicit assumption for performing a linear viscoelastic inversion in our study is the quasi-time-independent behavior of surface velocity in the late stage of the interseismic period. Without considering an initial earthquake, the Maxwell material exhibits constant viscoelastic response under constant interseismic loading. Hence, the velocity of surface displacement from an ideal viscoelastic seismic cycle model would remain constant after reaching the relaxation of the interseismic stress. In a numerical model the effect of initiating back slip on the fault will be diminished after about 20 times the Maxwell time (about 200 years) in a relaxed simulated system [*Hu et al.*, 2004]. Therefore, the stabilized velocities on the model surface in the late stages of simulation of for our model are likely due to the constant interseismic loading in a relaxed system (Figures S3 and S4).

In order to test the influence of a previous great earthquake on the late stage interseismic deformation in the following cycle, we carry out a simulation starting with an *Mw* 8.6 earthquake (by assuming a 200 km segment is ruptured) as well as constant back slip loading. This earthquake represents a total release of all accumulated slip deficit in an interface fully locked up to 50 km depth during a cycle of 100 years. The viscoelastic response of this earthquake diminishes to near zero 60 to 80 years after the earthquake (Figures S5 and S6). After 100 years of simulation time, the differences of the velocities between the earthquake and nonearthquake models are only a few millimeters per year, a value much less than uncertainties in the GPS velocity vectors. Moreover, displacements at surface points (ranging from 50 to 300 km away from the trench) show constant or quasi-constant displacement velocities in the final years of the cycle. This time that we calculated for previous earthquake effects becoming negligible is consistent with previous numerical studies [e.g., *Hu et al.*, 2004; *Wang et al.*, 2001, 2012]. Thus, by not starting with an initial great earthquake and simulating a total of 200 years of constant interseismic loading, the considered surface velocities in the last stage of simulation can capture well the quasi-time-independent behavior of steady state viscoelastic interseismic deformation in a relaxed system.

In nature, the subduction zone system earthquake recurrence time may vary from cycle to cycle, and therefore, the flow in the viscoelastic domains may never reach a steady state. One simple assumption that could be made is that the late interseismic deformation that we observe is repeated over many cycles. To achieve this assumption numerically, we can spin-up the model [e.g., *Hetland and Hager*, 2006], whereby the earthquake cycle is modeled enough times so that the consecutive late-interseismic deformation has the same spatiotemporal characteristics. Results of basic spin-up tests (Figure S9) show that the viscoelastic contribution of the horizontal deformation can differ by as much as 40% for spun-up and non-spun-up models. However, the assumption of perfect cyclical earthquake behavior, in both magnitude and lateral rupture extents, is a poor one, and therefore, we are satisfied with our current approach that does not assume a perfectly cyclical subduction stress release.

7.3. Interpretation of the GPS Measurements of Interseismic Deformation in Peru-North Chile Subduction Zone

The North Chile subduction zone has been described as a mature seismic gap, which remains unruptured by a $Mw > 8.5$ since the occurrence of the 1877 earthquake ($Mw \sim 8.8$ [*Comte and Pardo*, 1991]). The published GPS data that we use were collected in the late 1990s and 2010s, when the deformation due to the previous great earthquake is expected to have disappeared, as it shown by linear trends in the GPS time series [*Métois et al.*, 2013]. Hence, we do not deem it necessary to make an alternative model which considers the viscoelastic deformation of the previous earthquake.

By using elastic and viscoelastic forward models constrained by different uniform full locking depths, we find that viscoelastic models result in overall smaller WRMS misfits than elastic models, especially for GPS observations in the back arc. Elastic models require a deeper locking depth, especially to fit the far-field geodetic data, while a viscoelastic model can fit both near- and far-field data with a shallower locking depth (Figure 7), in agreement with results of our 2-D synthetic models (Figure 3). Results of forward models (Figure 2) highlight the sensitivity of the surface deformation to the downdip limit of the locked zone and the need of a viscoelastic model to produce a broadened deformation field. Patterns of residuals pointing to the trench (around 23°S, 20.5°S, and 18.5°S) from the elastic and viscoelastic models (Figure 8) indicate areas where a fully locked seismogenic zone overpredicts the observed velocities, suggesting the existence of along-strike variations of the locking degree. As we move further inland from the coast, residuals from the purely elastic model show a consistent pattern of underpredicted eastward motion (by ~10 mm/yr). This pattern of misfit extends into the back arc (69°W to 68°W) and represents the signal that has been previously interpreted using three-plate elastic models [*Chlieh*, 2011; *Métois et al.*, 2013] to characterize the back-arc shortening and Andean sliver motion. The viscoelastic model fits the back-arc displacements well, suggesting the Andean shortening or sliver deformation may be at present of lower magnitude than previously reported. Another physical inconsistency related to elastic models is the need for very deep locking [e.g., *Métois et al.*, 2013] (down to 80 km depth) to reproduce the long wave deformation signals in the back arc.

The modeling approach that we adopt for the case study of the Peru-North Chile subduction margin does not consider the motion of possible microplates (sliver motion) and back-arc shortening. Considerations of such microplate processes can significantly alter the final obtained locking estimation, and it is not a trivial exercise

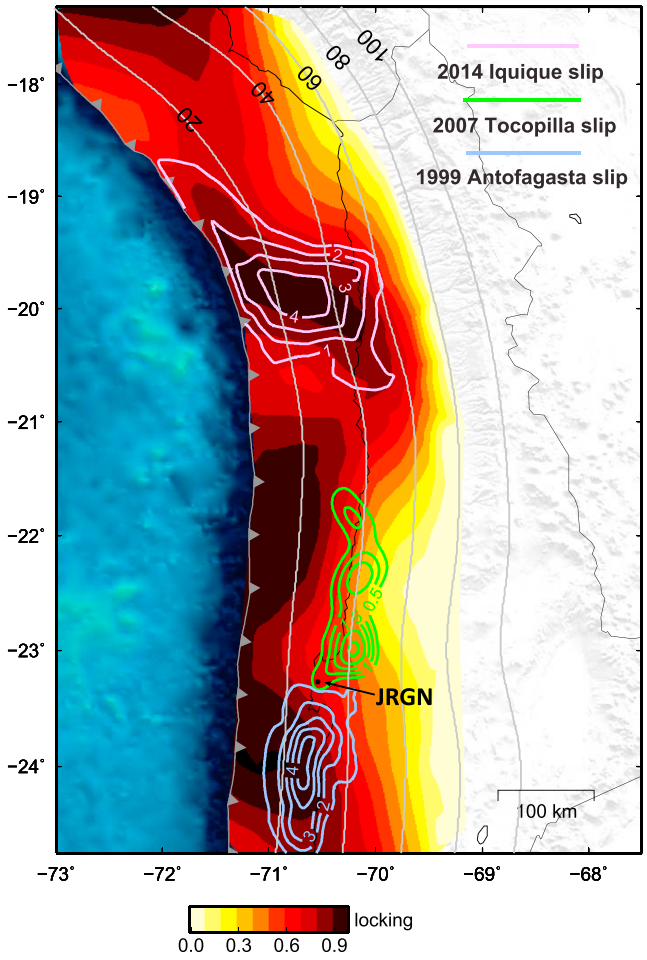

Figure 10. Comparison of our optimal viscoelastic locking map with the slip distributions of the 2014 Iquique earthquake (derived from our own FEM inversion), 2007 Tocopilla earthquake [*Schurr et al.*, 2012] and 1999 Antofagasta earthquake [*Chlieh et al.*, 2004]. The gray solid contours are the isodepths of the subduction interface (the values are given in kilometer).

to remove these effects from the data before inverting for locking [e.g., *Chlieh*, 2011; *Métois et al.*, 2013]. Therefore, the adoption of the viscoelastic Green's functions should lead to a reevaluation of these microplate corrections to the data before inversion. In this study we have shown for the interseismic deformation of the Peru-North Chile margin that sliver corrections are unnecessary if viscoelastic Green's functions are used.

The residuals of the elastic inversion show a pattern similar to the elastic forward model, i.e., large misfit in the back arc. Without back-arc shortening and sliver motion corrections, the elastic model needs a larger average back slip magnitude with little variation in locking degree in the along-strike direction (Figure 9b) when compared to the viscoelastic inversion results (Figure 9d). The elastic model shows gaps in locking between highly locked segments north of the Mejillones Peninsula (in between latitude 23°S to 24°S) and near the Chile-Peru border. The residuals of the viscoelastic model (Figure 9d) are much less than the residuals of the elastic model (Figure 9b), and the along margin segmentation of highly locked patches for the viscoelastic model is increased, with a low in locking becoming apparent at 20.8°S, which is not as pronounced in the elastic model.

We use a checkerboard synthetic back slip model to evaluate the model resolution and to demonstrate which features of the locking map can currently be resolved by the GPS data (Figure S10). The input locked patches are about 30 km in size and are assigned with a 67 mm/yr back slip rate (Figure S10b). The sizes of these input patches are similar to those of the creeping patches as found in our inversion results (Figure 9) as well as in similar locking studies [*Chlieh*, 2011; *Métois et al.*, 2013; *Schurr et al.*, 2014]. The elastic and viscoelastic models have similar recovery patterns. Both models give the best resolution under the coastline with resolution rapidly decreasing toward the trench and decreasing more gradually in the downdip direction (Figures S10a and S10c).

Our favored locking model is chosen to be the viscoelastic model and is shown in Figure 10 along with the slip distributions of the most recently observed large earthquakes in this margin. The two main locked patches are between latitudes 19°S and 21°S and south of 21°S.

7.4. Correlation of Historical Earthquake Slip Distributions With Locking Patterns From Viscoelastic Models

The spatial and temporal span of the GPS data is an important factor to consider in interpreting the relationship of the derived apparent locking degree and the slip distributions of historical ruptures. The most recent set of GPS velocities that is distributed mainly in fore-arc region [*Métois et al.*, 2013] (blue vectors in Figure 6) was acquired between 2008 and 2012. The older set of GPS observations of *Kendrick et al.* [2001] that spans

mainly the back arc as well as north of latitude 22°S in the fore arc (green vectors in Figure 6) was collected between 1993 and 2001. Hence, the apparent locking state around the rupture area of 2014 Iquique earthquake north of latitude 22°S was obtained by the combination of data from both the earlier and later data sets, while the locking state around the rupture area of the two previous earthquakes south of latitude 22°S was determined mainly by the data from latest data set. Therefore, the locking state around Iquique earthquake rupture zone was determined by GPS observations from the late stage of the interseismic period, whereas the locking state around Tocopilla and Antofagasta earthquake rupture zones was obtained by GPS observations that are potentially affected by postseismic signals.

The highly locked patch between latitudes 19°S and 21°S in Figure 10 clearly correlates very strongly with the coseismic slip distribution of the 2014 Iquique-Pisagua *Mw* 8.1 earthquake. The slip distribution shown is obtained from inversion of data corresponding to the main shock and *Mw* 7.6 aftershock of the Iquique-Pisagua earthquake from *Schurr et al.* [2014] and using our own FEM-derived elastic Green's functions (result shown in Figure S11). By using our own rather than previously published coseismic slip distributions, we facilitate a fairer spatial comparison to our locking model since we are using the same model configurations and boundary conditions. For the Iquique-Pisagua earthquake, there is a very good spatial correlation between a highly locked region and the slip extents of the main shock and largest aftershock ruptures. Moreover, the patch of locking extends in depth and southward in agreement with the aftershock propagation direction after the Iquique main event [*Schurr et al.*, 2014].

The Tocopilla rupture zone is thought to have been highly coupled up to a depth of 50 km before the 2007 event [*Chlieh et al.*, 2011]. This moderate size *Mw* 7.7 earthquake occurred in the deepest extents of the seismogenic zone [*Schurr et al.*, 2012] and should have increased the stress on the shallowest part of this zone. Hence, the locking degree near the rupture area of the 2007 earthquake appears to be low, while the degree of locking updip of this (which has not ruptured yet) is higher. Furthermore, the GPS vectors (collected more than 1 year after the earthquake) in the fore arc of this segment of the margin are almost the same magnitude as those at stations further north (Figure 6), where there is not expected to be any significant postseismic deformation. Therefore, the subduction interface here has probably completed the relocking process and the postseismic relaxation signals of this event are deemed insignificant, especially in the fore-arc region [*Wang et al.*, 2012]. Moreover, the time series at continuous GPS stations near Tocopilla and Mejillones Peninsula show that the postseismic deformation of the Tocopilla earthquake decayed rapidly (within less than 2 years) and seem to exhibit no postseismic deformation from the Tocopilla and Antofagasta earthquakes as previously pointed out by *Métois et al.* [2013]. For example, at the continuous JRGN station (near the coastline of Mejillones Peninsula shown as black dot in Figure 10), a weak postseismic transient signal is only recorded until early 2008, while after 2009 the displacements are steady and well fitted by a linear trend (Figure S12). Therefore, the locking pattern around Mejillones Peninsula (at the spatial limits of the Antofagasta and Tocopilla events) is not likely to be contaminated by any postseismic relaxation signal and represents an interface in the interseismic state. This pattern may be related to a long-term creeping barrier [e.g., *Métois et al.*, 2013] but also can be a temporal feature influenced by the postseismic processes of the Tocopilla and Antofagasta events.

8. Conclusion

In this study we show that the viscoelastic behavior of mantle contributes significantly to the interseismic surface deformation field, and therefore, this viscoelastic effect strongly influences the locking distribution modeled from geodetic observations. By first comparing the surface displacement difference between elastic and viscoelastic models with synthetic 2-D models, we demonstrate how the viscoelastic model can reproduce longer-wavelength interseismic deformation than the elastic model and then we present the evidence for this longer-wavelength deformation in the observed GPS data. By means of synthetic modeling we reveal the pitfalls of inverting viscoelastic interseismic deformation with elastic models: the most notable pitfall being that using a purely elastic model to invert horizontal GPS velocities for locking degree results in an overestimation of the true locking depth. By using Maxwell materials in the model, we detail a useful method for performing linear inversions of viscoelastic deformation based on FEM-derived Green's functions. The fully linear system allows a viscoelastic model inversion that can resolve slip details along the fault interface with little misfit between inversion result and synthetic observations.

Finally, we apply our methodology to a 3-D case study of Peru-North Chile, which includes the segment of the 2014 *Mw* 8.1 Iquique-Pisagua, using published GPS data of the late interseismic surface velocities in North Chile seismic gap. The viscoelastic models surpass the elastic models in fitting the GPS data, which suggests that the significant viscoelastic effects on interseismic deformation that we can model are observed in the GPS data. Moreover, the viscoelastic model provides a more realistic locking depth after data inversion, and this result is valid for both the whole data set and a subset including only the far-field stations. The elastic model can produce credible shallow locking depths but struggles to fit the far-field data. Furthermore, using elastic models to model the surface deformation requires an unrealistic deeper locking depth to improve fits to the far-field data. Remarkably, for the viscoelastic model, we are able to fit the data with a realistic locking depth without having to perform any preliminary data corrections for microplate motion. Therefore, previous locking estimations using a purely elastic model may be overestimating the contribution to the GPS velocities caused by microplate motions.

The locking pattern of the viscoelastic model has a better spatial correlation with the slip distributions of the *Mw* 8.1 main shock and *Mw* 7.6 aftershock of the Iquique-Pisagua earthquake than the previously published elastic model locking patterns. Our results thus suggest that it is necessary to reevaluate purely elastic models of locking in subduction zones, instead using Green's functions that consider the viscoelastic contribution to the late seismic-cycle surface velocities, to better estimate the likely rupture limits and magnitudes of future megathrust events.

Acknowledgments

Shaoyang Li gratefully acknowledges the scholarship granted to him by the China Scholarships Council (201206040055). Shaoyang Li is a member of the Helmholtz graduate research school GeoSim. Marcos Moreno and Jonathan Bedford have been supported by the MARISCOS project MO 2310/1-1. The authors would like to thank the main developers of the open source PyLith software for their ongoing dedication to the software development and generous technical support. The GPS data shown in this article are available from published paper *Métois et al.* [2013] and *Kendrick et al.* [2001]. This paper has benefitted from discussions with Jan Botle and Isabel Urrutia. We would like to thank the reviewers Kelin Wang and Charles Williams and Associate Editor Laura Wallace for their invaluable comments and suggestions. Some of the figures in this paper were created with GMT software [*Wessel and Smith*, 1998] and matplotlib module [*Hunter*, 2007].

References

Aagaard, B. T., M. G. Knepley, and C. A. Williams (2013), A domain decomposition approach to implementing fault slip in finite-element models of quasi-static and dynamic crustal deformation, *J. Geophys. Res. Solid Earth*, *118*, 3059–3079, doi:10.1002/jgrb.50217.

Angermann, D., J. Klotz, and C. Reigber (1999), Space-geodetic estimation of the Nazca-South America Euler vector, *Earth Planet. Sci. Lett.*, *171*, 329–334.

Bevis, M., E. Kendrick, R. J. Smalley, B. Brooks, R. Allmendinger, and B. Isacks (2001), On the strength of interplate coupling and the rate of back arc convergence in the central Andes: An analysis of the interseismic velocity field, *Geochem. Geophys. Geosyst.*, *2*, 1067, doi:10.1029/2001GC000198.

Brooks, B. (2003), Crustal motion in the Southern Andes (26°–36°S): Do the Andes behave like a microplate? *Geochem. Geophys. Geosyst.*, *4*(10), 1085, doi:10.1029/2003GC000505.

Brooks, B. A., et al. (2011), Orogenic-wedge deformation and potential for great earthquakes in the central Andean backarc, *Nat. Geosci.*, *4*(6), 380–383.

Bürgmann, R., M. G. Kogan, G. M. Steblov, G. Hilley, V. E. Levin, and E. Apel (2005), Interseismic coupling and asperity distribution along the Kamchatka subduction zone, *J. Geophys. Res.*, *110*, B07405, doi:10.1029/2005JB003648.

Chlieh, M. (2004), Crustal deformation and fault slip during the seismic cycle in the North Chile subduction zone, from Global Positioning System and InSAR observations, *Geophys. J. Int.*, *158*, 695–711.

Chlieh, M. (2011), Interseismic coupling and seismic potential along the Central Andes subduction zone, *J. Geophys. Res.*, *116*, B12405, doi:10.1029/2010JB008166.

Chlieh, M., J. B. De Chabalier, J. C. Ruegg, R. Armijo, R. Dmowska, J. Campos, and K. L. Feigl (2004), Crustal deformation and fault slip during the seismic cycle in the North Chile subduction zone, from GPS and InSAR observations, *Geophys. J. Intl.*, *158*(2), 695–711.

Chlieh, M., et al. (2011), Interseismic coupling and seismic potential along the Central Andes subduction zone, *J. Geophys. Res.*, *116*, B12405, doi:10.1029/2010JB008166.

Christensen, R. (1982), *Theory of Viscoelasticity: An Introduction*, Elsevier Science, Oxford.

Coleman, T. F., and Y. Li (1996), A reflective Newton method for minimizing a quadratic function subject to bounds on some of the variables, *SIAM J. Optim.*, *6*(4), 1040–1058, doi:10.1137/S1052623494240456.

Comte, D., and M. Pardo (1991), Reappraisal of great historical earthquakes in the northern Chile and southern Peru seismic gaps, *Nat. Hazards*, *4*(1), 23–44, doi:10.1007/bf00126557.

Comte, D., M. Pardo, L. Dorbath, C. Dorbath, H. Haessler, L. Rivera, A. Cisternas, and L. Ponce (1994), Determination of seismogenic interplate contact zone and crustal seismicity around Antofagasta, northern Chile using local data, *Geophys. J. Int.*, *116*(3), 553–561, doi:10.1111/j.1365-246X.1994.tb03279.x.

Contreras-Reyes, E., and A. Osses (2010), Lithospheric flexure modelling seaward of the Chile trench: Implications for oceanic plate weakening in the Trench Outer Rise region, *Geophys. J. Int.*, *182*(1), 97–112, doi:10.1111/j.1365-246X.2010.04629.x.

Du, Y., A. Aydin, and P. Segall (1992), Comparison of various inversion techniques as applied to the determination of a geophysical deformation model for the 1983 Borah Peak earthquake, *Bull. Seismol. Soc. Am.*, *82*(4), 1840–1866.

Freed, A. M., and R. Burgmann (2004), Evidence of power-law flow in the Mojave desert mantle, *Nature*, *430*(6999), 548–551.

Groß, K., U. Micksch, and S. T. TIPTEQ Research Group (2008), The reflection seismic survey of project TIPTEQ—The inventory of the Chilean subduction zone at 38.2°S, *Geophys. J. Int.*, *172*(2), 565–571, doi:10.1111/j.1365-246X.2007.03680.x.

Haberland, C., A. Rietbrock, D. Lange, K. Bataille, and T. Dahm (2009), Structure of the seismogenic zone of the south-central Chilean margin revealed by local earthquake traveltime tomography, *J. Geophys. Res.*, *114*, B01317, doi:10.1029/2008JB005802.

Harris, R. A., and P. Segall (1987), Detection of a locked zone at depth on the Parkfield, California, segment of the San Andreas Fault, *J. Geophys. Res.*, *92*(B8), 7945–7962, doi:10.1029/JB092iB08p07945.

Hayes, G. P., D. J. Wald, and R. L. Johnson (2012), Slab1.0: A three-dimensional model of global subduction zone geometries, *J. Geophys. Res.*, *117*, B01302, doi:10.1029/2011JB008524.

Hayes, G. P., M. W. Herman, W. D. Barnhart, K. P. Furlong, S. Riquelme, H. M. Benz, E. Bergman, S. Barrientos, P. S. Earle, and S. Samsonov (2014), Continuing megathrust earthquake potential in Chile after the 2014 Iquique earthquake, *Nature*, *512*(7514), 295–298.

Hetland, E. A., and B. H. Hager (2006), Interseismic strain accumulation: Spin-up, cycle invariance, and irregular rupture sequences, *Geochem. Geophys. Geosyst.*, *7*, Q05004, doi:10.1029/2005GC001087.

Hindle, D., J. Kley, E. Klosko, S. Stein, T. Dixon, and E. Norabuena (2002), Consistency of geologic and geodetic displacements during Andean orogenesis, *Geophys. Res. Lett.*, *29*(8), 1188, doi:10.1029/2001GL013757.
Hu, Y., K. Wang, J. He, J. Klotz, and G. Khazaradze (2004), Three-dimensional viscoelastic finite element model for postseismic deformation of the great 1960 Chile earthquake, *J. Geophys. Res.*, *109*, B12403, doi:10.1029/2004JB003163.
Hu, Y., R. Burgmann, J. Freymueller, P. Banerjee, and K. Wang (2014), Contributions of poroelastic rebound and a weak volcanic arc to the postseismic deformation of the 2011 Tohoku earthquake, *Earth Planets Space*, *66*(1), 1–10, doi:10.1186/1880-5981-66-106.
Hunter, J. D. (2007), Matplotlib: A 2D graphics environment, *Comput. Sci. Eng.*, *9*(3), 0090–0095.
Hyndman, R. D., and K. Wang (1993), Thermal constraints on the zone of major thrust earthquake failure: The Cascadia Subduction Zone, *J. Geophys. Res.*, *98*(B2), 2039–2060, doi:10.1029/92JB02279.
Ivins, E. R., and T. S. James (1999), Simple models for late Holocene and present-day Patagonian glacier fluctuations and predictions of a geodetically detectable isostatic response, *Geophys. J. Int.*, *138*(3), 601–624, doi:10.1046/j.1365-246x.1999.00899.x.
Kanda, R. V. S., and M. Simons (2010), An elastic plate model for interseismic deformation in subduction zones, *J. Geophys. Res.*, *115*, B03405, doi:10.1029/2009JB006611.
Kendrick, E. (2003), The Nazca-South America Euler Vector and its rate of change, *J. S. Am. Earth. Sci.*, *16*, 125–131.
Kendrick, E., M. Bevis, R. Smalley, and B. Brooks (2001), An integrated crustal velocity field for the Central Andes, *Geochem. Geophys. Geosyst.*, *2*, 1066, doi:10.1029/2001GC000191.
Kirby, S. H., and A. K. Kronenberg (1987), Rheology of the lithosphere: Selected topics, *Rev. Geophys.*, *25*, 1219–1244, doi:10.1029/RG025i006p01219.
Li, S., M. Moreno, M. Rosenau, D. Melnick, and O. Oncken (2014), Splay fault triggering by great subduction earthquakes inferred from finite-element models, *Geophys. Res. Lett.*, *41*, 385–391, doi:10.1002/2013GL058598.
Masterlark, T. (2003), Finite element model predictions of static deformation from dislocation sources in a subduction zone: Sensitivities to homogeneous, isotropic, Poisson-solid, and half-space assumptions, *J. Geophys. Res.*, *108*(B11), 2540, doi:10.1029/2002JB002296.
Masterlark, T., and K. L. H. Hughes (2008), Next generation of deformation models for the 2004 M9 Sumatra-Andaman earthquake, *Geophys. Res. Lett.*, *35*, L19310, doi:10.1029/2008GL035198.
McCaffrey, R. (2002), Crustal block rotations and plate coupling, *Plate Bound. Zones*, 101–122.
Métois, M., A. Socquet, C. Vigny, D. Carrizo, S. Peyrat, A. Delorme, E. Maureira, M.-C. Valderas-Bermejo, and I. Ortega (2013), Revisiting the North Chile seismic gap segmentation using GPS-derived interseismic coupling, *Geophys. J. Int.*, doi:10.1093/gji/ggt183.
Mitrovica, J. X. (1996), Haskell [1935] revisited, *J. Geophys. Res.*, *101*, 555–569, doi:10.1029/95JB03208.
Moreno, M. S., J. Bolte, J. Klotz, and D. Melnick (2009), Impact of megathrust geometry on inversion of coseismic slip from geodetic data: Application to the 1960 Chile earthquake, *Geophys. Res. Lett.*, *36*, L16310, doi:10.1029/2009GL039276.
Moreno, M., M. Rosenau, and O. Oncken (2010), Maule earthquake slip correlates with pre-seismic locking of Andean subduction zone, *Nature*, *467*, 198–202.
Moreno, M., et al. (2011), Heterogeneous plate locking in the South–Central Chile subduction zone: Building up the next great earthquake, *Earth Planet. Sci. Lett.*, *305*(3–4), 413–424, doi:10.1016/j.epsl.2011.03.025.
Nocquet, J. M., et al. (2011), Motion of continental slivers and creeping subduction in the northern Andes, *Nat. Geosci.*, *7*(4), 287–291.
Okada, Y. (1985), Surface deformation due to shear and tensile faults in a half-space, *Bull. Seismol. Soc. Am.*, *75*, 1135–1154.
Okada, Y. (1992), Internal deformation due to shear and tensile faults in a half-space, *Bull. Seismol. Soc. Am.*, *82*, 1018–1040.
Oncken, O., D. Boutelier, G. Dresen, and K. Schemmann (2012), Strain accumulation controls failure of a plate boundary zone: Linking deformation of the Central Andes and lithosphere mechanics, *Geochem. Geophys. Geosyst.*, *13*, Q12007, doi:10.1029/2012GC004280.
Peltier, W. R., P. Wu, and D. A. Yuen (1981), The viscosities of the Earth's mantle, in *Anelasticity in the Earth*, edited, pp. 59–77, AGU, Washington D. C., doi:10.1029/GD004p0059.
Pollitz, F. F., R. Burgmann, and P. Banerjee (2006), Post-seismic relaxation following the great 2004 Sumatra-Andaman earthquake on a compressible self-gravitating Earth, *Geophys. J. Int.*, *167*(1), 397–420, doi:10.1111/j.1365-246X.2006.03018.x.
Pollitz, F., P. Banerjee, K. Grijalva, B. Nagarajan, and R. Burgmann (2008), Effect of 3-D viscoelastic structure on post-seismic relaxation from the 2004 M = 9.2 Sumatra earthquake, *Geophys. J. Int.*, *173*, 189–204.
Reid, H. F. (1910), *The Mechanics of the Earthquake*, Carnegie Institution of Washington, Washington, D. C.
Ruegg, J. C., A. Rudloff, C. Vigny, R. Madariaga, J. B. de Chabalier, J. Campos, E. Kausel, S. Barrientos, and D. Dimitrov (2009), Interseismic strain accumulation measured by GPS in the seismic gap between Constitución and Concepción in Chile, *Phys. Earth Planet. Int.*, *175*(1–2), 78–85, doi:10.1016/j.pepi.2008.02.015.
Savage, J. (1983), A dislocation model of strain accumulation and release at a subduction zone, *J. Geophys. Res.*, *88*, 4984–4996, doi:10.1029/JB088iB06p04984.
Schurr, B., A. Asch, F. Sodoudi, A. Manzanares, O. Ritter, J. Klotz, G. Chong-Diaz, S. Barrientos, J.-P. Villotte, and O. Oncken (2009), The International Plate Boundary Observatory Chile (IPOC) in the northern Chile seismic gap, paper presented at EGU General Assembly Conference Abstracts.
Schurr, B., G. Asch, M. Rosenau, R. Wang, O. Oncken, S. Barrientos, P. Salazar, and J. P. Vilotte (2012), The 2007 M7.7 Tocopilla northern Chile earthquake sequence: Implications for along-strike and downdip rupture segmentation and megathrust frictional behavior, *J. Geophys. Res.*, *117*, B05305, doi:10.1029/2011JB009030.
Schurr, B., et al. (2014), Gradual unlocking of plate boundary controlled initiation of the 2014 Iquique earthquake, *Nature*, *512*(7514), 299–302, doi:10.1038/nature13681.
Sun, T., et al. (2014), Prevalence of viscoelastic relaxation after the 2011 Tohoku-oki earthquake, *Nature*, *514*(7520), 84–87.
Tassara, A., and A. Echaurren (2012), Anatomy of the Andean subduction zone: Three-dimensional density model upgraded and compared against global-scale models, *Geophys. J. Int.*, *189*(1), 161–168, doi:10.1111/j.1365-246X.2012.05397.x.
Thatcher, W., and J. B. Rundle (1984), A viscoelastic coupling model for the cyclic deformation due to periodically repeated earthquakes at subduction zones, *J. Geophys. Res.*, *89*, 7631–7640, doi:10.1029/JB089iB09p07631.
Wallace, L. M., J. Beavan, R. McCaffrey, and D. Darby (2004), Subduction zone coupling and tectonic block rotations in the North Island, New Zealand, *J. Geophys. Res.*, *109*, B12406, doi:10.1029/2004JB003241.
Wang, K., J. He, H. Dragert, and T. James (2001), Three-dimensional viscoelastic interseismic deformation model for the Cascadia subduction zone, *Earth Planets Space*, *53*(4), 295–306, doi:10.1186/bf03352386.
Wang, K., Y. Hu, and J. He (2012), Deformation cycles of subduction earthquakes in a viscoelastic Earth, *Nature*, *484*(7394), 327–332.
Wessel, P., and W. H. F. Smith (1998), New, improved version of the Generic Mapping Tools released, *Eos Trans. AGU*, *79*, 579, doi:10.1029/98EO00426.
Yuan, X., et al. (2000), Subduction and collision processes in the Central Andes constrained by converted seismic phases, *Nature*, *408*(6815), 958–961.